



Spectroscopic investigations of a Ti : Tm : LiNbO₃ waveguide for photon-echo quantum memory

N. Sinclair^{a,*}, E. Saglamyurek^{a,1}, M. George^b, R. Ricken^b, C. La Mela^{a,2}, W. Sohler^b, W. Tittel^a

^a Institute for Quantum Information Science and Department of Physics & Astronomy, University of Calgary, Calgary, Alberta, Canada T2N 1N4

^b Angewandte Physik, Universität Paderborn, 33098 Paderborn, Germany

ARTICLE INFO

Available online 23 December 2009

Keywords:

Rare-earth-ion doped crystals
LiNbO₃ waveguides
Photon-echo
Spectral hole burning
Optical coherence
Quantum communication
Quantum memory

ABSTRACT

We report the fabrication and characterization of a Ti⁴⁺:Tm³⁺:LiNbO₃ optical waveguide in view of photon-echo quantum memory applications. Specifically, we investigated room- and cryogenic-temperature properties of the waveguide, and the Tm³⁺ ions, via absorption, spectral hole burning, photon echo, and Stark spectroscopy. For the Tm³⁺ ions, we found radiative lifetimes of 82 μs and 2.4 ms for the ³H₄ and ³F₄ levels, respectively, and a 44% branching ratio from the ³H₄ to the ³F₄ level. We also measured an optical coherence time of 1.6 μs for the ³H₆ ↔ ³H₄, 795 nm wavelength transition, and investigated the limitation of spectral diffusion to spectral hole burning. Upon application of magnetic fields of a few hundred Gauss, we observed persistent spectral holes with lifetimes up to seconds. Furthermore, we measured a linear Stark shift of 25 kHz/cm/V. Our results are promising for integrated, electro-optical, waveguide quantum memory for photons.

© 2009 Elsevier B.V. All rights reserved.

1. Introduction

Quantum memory constitutes a key element for quantum repeaters [1], as well as linear optical quantum computing [2]. Impressive experimental and theoretical progress has been reported over the past few years [3,4], and gives hope that a workable quantum memory can eventually be built.

The *photon-echo quantum memory* [5] is based on all-optical storage of classical data, investigated originally thirty years ago [6–9]. It relies on the interaction of light with a large ensemble of atoms with a suitably prepared, inhomogeneously broadened absorption line. In materials with natural broadening, this tailoring can be achieved by frequency-selectively removing absorbers from the ground state to an auxiliary state using optical pumping techniques [10–13], possibly followed by controlled broadening of the resulting absorption lines, e.g. through position dependent Stark shifts.

The absorption of light in a photon-echo quantum memory leads to mapping of its quantum state onto collective atomic coherence, which rapidly decays as the absorbers have different resonance frequencies. To recall the light, i.e. map the quantum state back onto light, the initial coherence has to be re-

established. Two possibilities have been identified: In *Controlled Reversible Inhomogeneous Broadening* (CRIB), the detuning of each absorber with respect to the light carrier frequency has to be inverted [14–17]. Another possibility is to tailor the initial absorption line into an *Atomic Frequency Comb* (AFC), resulting in re-emission of the stored light after a time that depends on the periodicity of the comb [6,18,19]. In both approaches, the memory efficiency can theoretically reach 100% [14,17,18,20]. For extended storage in CRIB or AFC (then also allowing for on-demand recall), the excited atomic coherence can be transferred temporarily to longer-lived coherence, e.g. between hyperfine ground states. This reversible mapping of coherence can be achieved by means of two π-pulses [21], or via a direct Raman transfer [22–25].

Rare-earth-ion doped crystals (RE crystals) are promising material candidates for photon-echo quantum memories [5]. Key findings include the storage of qubit states encoded into attenuated laser pulses [19], light storage with up to 66% efficiency [20,26–28], mapping of photonic quantum states onto collective atomic spin states [21], and simultaneous storage of 64 photon modes [29]. Furthermore, observation of a coherence time of more than 30 s for a ground state hyperfine transition in Pr : Y₂SiO₅ [30] is highly promising for long-term storage in this crystal, as well as other RE crystals.

In this article we investigate a novel storage medium, a Ti⁴⁺:Tm³⁺:LiNbO₃ optical waveguide, in view of the requirements for photon-echo quantum memory. This material combines interesting features arising from the specific RE dopant, the host material, as well as the waveguide structure.

* Corresponding author. Tel.: +1 403 2107693.

E-mail address: nsinclair@qis.ucalgary.ca (N. Sinclair).

¹ These authors contributed equally to this work.

² Current address: Department of Engineering Physics, École Polytechnique de Montréal, Montréal, Québec, Canada H3C 3A7.

As depicted in Fig. 1, the thulium (Tm) $^3H_6 \leftrightarrow ^3H_4$ transition features absorption at ~ 795 nm, which is a wavelength where air has minimal transmission loss, where photon pairs or entangled photon pairs are conveniently created [31–34], and where high-efficiency and simple-to-operate single photon detectors based on Silicon Avalanche Photodiodes are commercially available [35]. This makes thulium-based quantum memories interesting for applications in quantum communication and linear optical quantum computing. Furthermore, the 3F_4 bottleneck state, whose energy is roughly half way between the 3H_6 and 3H_4 levels [36], allows for efficient and broadband spectral tailoring [37]. In addition, the application of suitably oriented magnetic fields has been reported to result in long-lived nuclear spin levels forming Λ systems (e.g. in Tm:YAG), which may be used for optical pumping or long-term storage [38–43].

Low-temperature spectroscopic investigations of Tm doped crystals have so far mostly concentrated on Tm:YAG (see also Ref. [44]) and, very recently, Tm : LiNbO₃ [45–48]. For Tm:YAG, they have already led to implementations of the AFC protocol [26,49].

Due to their lack of inversion symmetry, lithium niobate (LiNbO₃) crystals feature non-linear effects [50]. The crystal symmetry also results in permanent electric dipole moments for RE states, i.e. the possibility to externally control resonance frequencies via Stark shifts [51,52], as required for CRIB. Low-temperature properties of RE doped LiNbO₃ have been characterized in Refs. [46,47,52–54], e.g. for the development of radio-frequency analyzers [55].

Given its non-linear properties, LiNbO₃ has become an important material for the telecommunication industry. Procedures to implement waveguides, either through proton exchange [56], or titanium indiffusion [57], have been developed, allowing for simple integration with fiber-optics components. In addition, given their small transverse dimensions of 5–10 μm (depending on the light wavelength), traveling wave electrodes can be spaced closely, resulting in commercial intensity and phase modulators with switching (π) voltages of only a few volts, and switching times below 100 picoseconds [58]. Furthermore, as light intensities inside these waveguides can be very large, strong non-linear interactions are possible, including frequency up-conversion of photons [59]. For photon-echo quantum memory, these properties promise simple integration with fiber quantum networks, sub-nanosecond Stark shifting, and large Rabi frequencies, which will benefit optical pumping procedures. LiNbO₃ waveguides have been used for studies relevant to quantum memory in [52,60–62].

The remainder of this article is structured as follows: In Section 2, we describe and characterize the fabrication process of the waveguide. Next, in Section 3, we discuss polarization dependent absorption profiles measured at room and cryogenic temperatures. After a description of the experimental setup used for all following low-temperature measurements in Sections 4.1 and 4.2 focuses on relevant radiative lifetimes and branching ratios. Our investigations of optical coherence times, and the

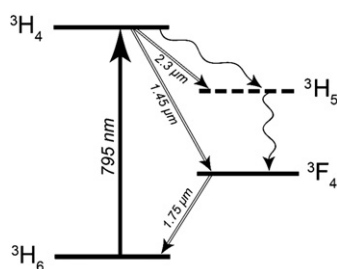


Fig. 1. Simplified energy level diagram of Tm : LiNbO₃ showing the electronic levels relevant to this work.

limitation of spectral hole burning imposed by spectral diffusion are presented in Section 4.3, followed by Stark-effect-based modification of narrow absorption lines. Finally, in Section 5, we discuss our results in view of photon-echo quantum memory. This concludes the article.

2. Waveguide fabrication and characterization

Tm-diffusion doping of LiNbO₃: Commercially available 0.5 mm thick Z-cut wafers of undoped optical grade congruent lithium niobate (CLN) were used as the starting material. Samples of 12 mm \times 30 mm size were cut from these wafers and doped by thulium near the +Z-surface before waveguide fabrication. The doping was achieved by in-diffusing a vacuum deposited (electron-beam evaporated) Tm layer of 19.6 nm thickness. The diffusion was performed at 1130 °C during 150 h in an argon-atmosphere followed by a post-treatment in oxygen (1 h) to get a full re-oxidization of the crystal.

To determine the diffusion coefficient of Tm into Z-cut CLN, secondary neutral mass spectroscopy (SNMS) was performed using 700 eV Argon-ions for ion milling. Ions and electrons were extracted from the plasma source with a duty cycle of 4:1 at a rate of 320 kHz to avoid charging of the insulating CLN-substrate. SNMS was chosen instead of secondary ion mass spectroscopy (SIMS) to significantly reduce matrix effects (see e.g. [63]). In Fig. 2, the concentration profiles versus depth have been recorded for thulium (Tm), lithium (Li), niobium (Nb) and oxygen (O). Interestingly, the Li-concentration slightly increases towards the surface, although it is expected that Tm occupies regular Li-sites similar to Er-ions when incorporated in CLN by diffusion [64].

In Fig. 3, the Tm concentration is plotted on a linear scale versus the depth. The slight dip close to the surface is unexpected and needs further investigations. Fitting a Gaussian profile to the concentration curve leads to a $1/e$ -penetration depth $d_{1/e}$ of about 6.5 μm . Together with the diffusion parameters, a diffusion coefficient $D = d_{1/e}^2/(4t) = 0.07 \mu\text{m}^2/\text{h}$, where t denotes the diffusion time, was evaluated for 1130 °C. At this temperature, this is seven times larger than the corresponding coefficient for Erbium-diffusion into CLN [65]. The maximum Tm concentration of about $1.35 \times 10^{20} \text{cm}^{-3}$ corresponds to a concentration 0.74 mole%, which—according to Ref. [64]—is considerably below the solid solubility of Tm in CLN.

Ti-indiffused waveguides in Tm:LiNbO₃: On the Tm-diffusion doped surface of the substrate, a 40 nm thick titanium (Ti) layer was deposited using electron-beam evaporation. From this layer, 3.0 μm wide Ti stripes were photolithographically defined and subsequently in-diffused at 1060 °C for 5 h to form 30 mm long optical strip waveguides. In the wavelength range around 775 nm, the waveguides are single mode for TE- and TM-polarization (see Fig. 3).

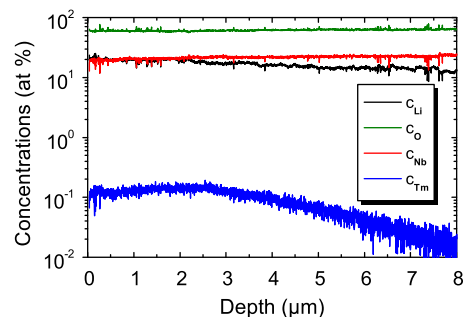


Fig. 2. Measured concentrations of Tm, Li, Nb, and O versus depth, using SNMS with 700 eV Ar-ions.

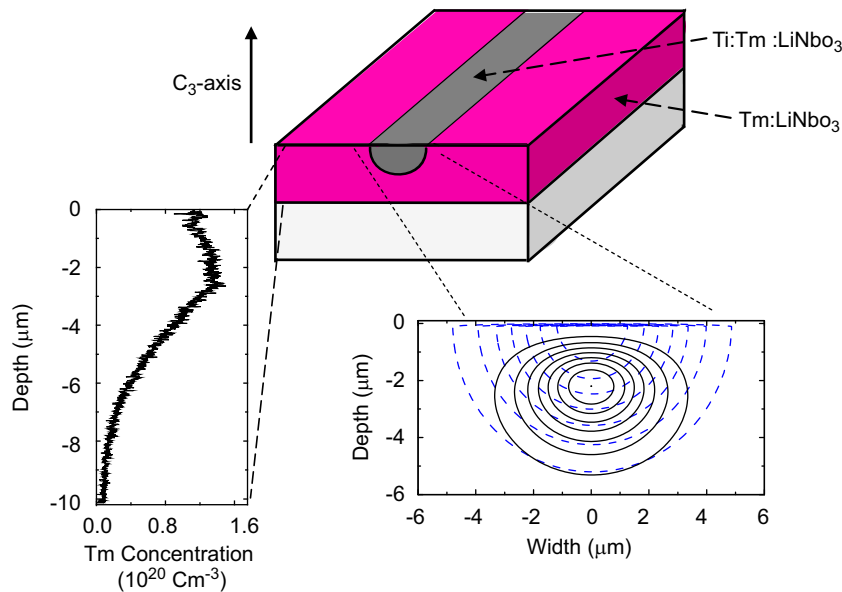


Fig. 3. Scheme of the waveguide geometry with the measured Tm concentration profile (on the left), and the calculated intensity distribution of the fundamental TM-mode superimposed on the profile of the extraordinary index of refraction induced by the Ti-doping (on the right). The latter data are calculated for 795 nm wavelength. Isolines denote 100%, 87.5%, 75% etc. of the maximum index increase ($\Delta n_{\max} = 4.0 \times 10^{-3}$), and the maximum mode intensity.

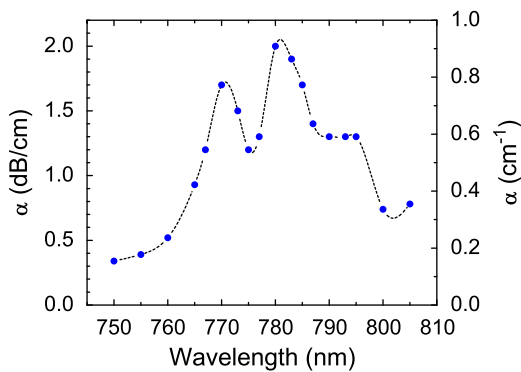


Fig. 4. Measured loss coefficient (α) for TM-polarization as a function of wavelength. Data points are connected by spline fitting as a guide for the eye.

The waveguide end faces were carefully polished normal to the waveguide axis, forming a low-finesse resonator. This allows to determine the total waveguide propagation loss at room temperature, including absorption and scattering loss, by the Fabry–Perot method [66]. A stabilized, single frequency Ti:Sapphire laser was used to measure the transmission of the low-finesse waveguide resonator as function of a small temperature change at a number of fixed wavelengths in the range between 750 and 807 nm. From the contrast of the measured Fabry–Perot response, the propagation loss was deduced for all wavelengths [66]. The results are presented in Fig. 4 for TM-polarization.

In addition, the waveguide propagation loss was determined at room temperature and 729 nm wavelength, where negligible absorption by the Tm-ions can be expected. Therefore, the measured loss coefficients reflect the scattering loss alone; they are 0.2 dB/cm for TE- as well as for TM-polarization. As the scattering loss is only weakly dependent on the wavelength, it can be regarded as a background for the Tm-induced absorption loss.

We repeated the off-resonant, polarization dependent loss measurement at 3.5 K, leading to strongly polarization dependent transmission. The exact origin of this difference compared to the room-temperature measurement requires further investigation.

For this as well as all subsequent low-temperature measurements, the sample was cut to 15.7 mm and repolished. All room-temperature measurements have been performed using a 30 mm long waveguide.

3. Spectroscopy of inhomogeneous broadening

Reversible atom-light interaction requires absorption on the transition between the lowest lying Stark levels in the ground and excited electronic states. To gain information about 3H_4 and 3H_6 Stark splittings, we injected weak, broadband, polarized light into the waveguide. Using wave plates, we set the polarization to TE or TM, and measured power spectra of the transmitted light using an optical spectrum analyzer (Anritsu MS9710C).

Room temperature characterization: The transmission through a 30 mm long waveguide for TE and TM-polarized light is shown in Fig. 5. It has been normalized to the incident spectral power density of the broadband tungsten lamp used in this experiment. We observe broad absorption, reflecting different transitions between Stark levels in the 3H_6 and 3H_4 multiplets (superimposed with inhomogeneous broadening), and the thermal distribution of the population in the electronic ground state. In addition, a strong polarization dependence of absorption is observed, confirming previous studies performed on bulk crystals [45,67].

Low temperature characterization: A similar measurement at 3.5 K resulted, for close-to TM polarization, in the absorption profile shown in the inset of Fig. 6. Due to the large optical depth of our sample, reflecting redistribution of population in the ground state Stark levels, we observe an almost flat-lined spectrum.

To resolve the Stark splittings, coherent laser light (Toptica DL 100) was coupled into the waveguide, and its frequency was swept between 791 and 796 nm in 0.1 nm steps. The laser intensity was optimized to resolve different Stark transitions after having partially bleached the absorption line. The resulting optical depth, shown in the main plot of Fig. 6, was determined at each measured wavelength upon normalization to the probe light. Using results from [48,68], we can identify four transitions

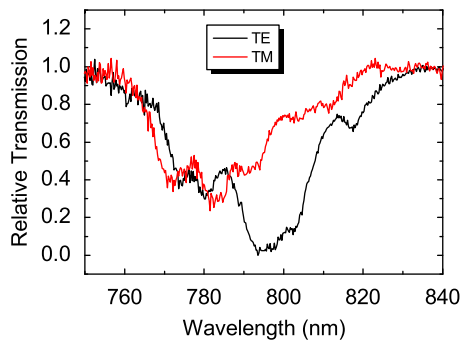


Fig. 5. Relative transmission through the Ti : Tm : LiNbO₃ waveguide for TM- and TE-polarization as a function of wavelength. The resolution bandwidth of the optical spectrum analyzer used in this experiment was 2 nm due to the low spectral power density of the thermal radiator.

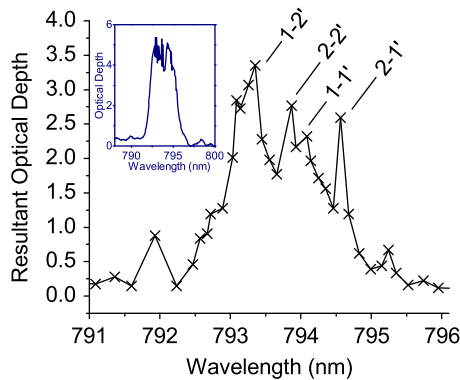


Fig. 6. Main figure: Absorption profile (after partial bleaching) at 3.5 K obtained using a single frequency laser. Indicated are transitions between different Stark levels: 1 and 2 denote the lowest energy levels within the ³H₆ multiplet, primed labels represent the lowest ³H₄ levels. Inset: The same inhomogeneous broadening probed using weak broadband light.

between the ground and excited state Stark multiplets, with splittings of 0.48 ± 0.05 and 0.93 ± 0.05 nm, respectively (i.e. 7.6 ± 0.8 and 14.7 ± 0.8 cm⁻¹, respectively). This indicates the presence of a zero-phonon line in the high wavelength region. According to calculations taking into account the observed splittings, only a small fraction of atomic population, $\sim 1\%$, occupies higher energy Stark levels of the ground state multiplet.

4. Narrow-band spectroscopic investigations

4.1. Experimental setup

A schematic of the experimental setup used for the low-temperature spectroscopic measurements described hereafter is depicted in Fig. 7.

A continuous wave, external cavity diode laser (Toptica DL 100) was tuned to 795.520 nm wavelength, where we found optical coherence properties of our sample in the absence of a magnetic field to be promising. The laser's linearly polarized output was amplified (Toptica BoosTA), and frequency and intensity modulated using a 400 MHz acousto-optic modulator (Brimrose TEM-400-100-793) in a double-pass configuration, driven by a 10 GS/s arbitrary waveform generator (Tektronix AWG7102) and an amplifier (Mini-circuits ZHL-5W-1). This allowed the creation of optical pulses with peak powers up to ~ 4 mW and durations between 20 ns and 500 ms for photon-echo sequences and spectral hole burning. Here and henceforth,

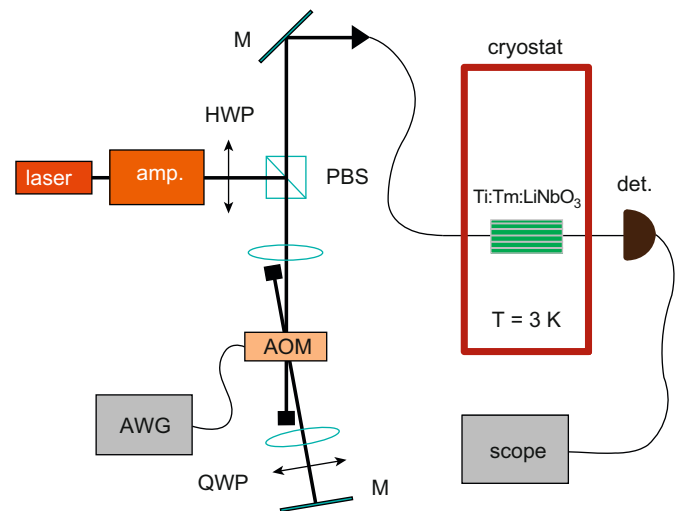


Fig. 7. Schematic of the experimental setup used for the narrow-band measurements at cryogenic temperature. HWP: half-wave plate; QWP: quarter-wave plate; PBS: polarization beam splitter; AOM: acousto-optic modulator; AWG: arbitrary waveform generator; M: mirror; amp.: optical amplifier; det.: detector; scope: oscilloscope.

all pulse powers are specified at the input of the cryostat. After passing a $\lambda/2$ wave plate, the light was coupled into a single-mode optical fiber, and sent into the 3.5 μ m wide, single mode Ti: Tm: LiNbO₃ waveguide. The light's polarization, which could be partially controlled using the wave plate, was set as to maximize the transmission, i.e. as to minimize the distance to TM. To inject and retrieve the light from the waveguide, optical fibers were butt-coupled against its front and end face using high precision translation stages (Attocube ANP100), resulting in fiber-to-fiber coupling loss around 15 dB. The waveguide was placed in a pulse tube cooler (Vericold VT4) and cooled to 3 K. A superconducting coil allowed the generation of magnetic fields along the crystal's C₃-axis, and electric fields could be generated along the same direction using aluminum electrodes that were firmly pressed against the crystal. Transmitted pulses and echoes were detected using either a sensitive 10 MHz (New Focus 2051), or a fast 125 MHz (New Focus 1801) photodetector, which was then connected to a 3 GHz bandwidth oscilloscope with 10 GS/s sampling rate (LeCroy wavepro 7300A). All measurements conducted at zero magnetic field were repeated every 100 ms, and generally averaged 300 times. Upon magnetic field application, the repetition period was set to 60 s, which was required to avoid accumulation effects, and the number of averages was reduced to 25.

4.2. Population relaxation dynamics

To optimize optical pumping strategies, and determine possibilities for long-term storage, it is important to examine the relaxation avenues and population dynamics in atomic levels involved in the light-atom interaction. The level scheme for thulium doped crystals in the case of zero magnetic field is depicted in Fig. 1. Upon excitation of the lowest lying Stark level within the ³H₄ manifold, atoms will eventually decay back to the ground state, either directly, or via the ³H₅ and ³F₄ levels. As the radiative lifetime of the ³H₅ level is short compared to the lifetimes of the ³H₄ and ³F₄ levels [45], we model atomic decay, i.e. radiative lifetimes and branching ratio (given by the rate of decay from ³H₄ to ³F₄ relative to the overall decay from ³H₄), using a simplified three-level scheme comprising only the ³H₆ ground state, the ³F₄ bottleneck state, and the ³H₄ excited state.

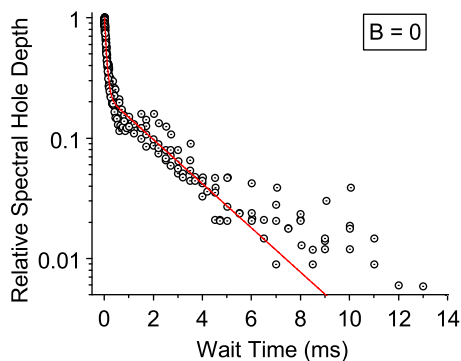


Fig. 8. Spectral hole decay under zero magnetic field. Plotted circles denote the normalized spectral hole depth as a function of the waiting time between burning and reading pulses. Two exponential decays are easily identified, yielding radiative lifetimes of 82 μ s and 2.4 ms for the 3H_4 and 3F_4 levels, respectively. The branching ratio into the 3F_4 level is approximately 44%.

As material absorption is dependent upon population differences between the states coupled by the probe light, we can assess population dynamics through time-resolved spectral hole burning. To this end, we first transfer population to the excited state using a 5–10 μ s long *burning* pulse with peak power of 7 μ W, and then probed the shape and depth of the created spectral hole after a *waiting time* ranging from 10 μ s to 15 ms using a chirped *reading* pulse. The power of the reading pulse, around 1 μ W, was chosen as to not alter the population distribution created by the burning pulse. Fig. 8 depicts the time dependent depth of the spectral hole, which we found to be proportional to the hole area (i.e. the effect of spectral diffusion, leading to a waiting-time-dependent hole width, was not visible in this measurement).

We model the decay using three-level rate equations, leading to

$$\frac{\Delta d(t)}{\Delta d(0)} = (1-B)e^{-t/T_{1e}} + Be^{-t/T_{1b}} \quad (1)$$

where $\Delta d(t)$ denotes the reduction of optical depth $d = \alpha L$ at the center of the spectral hole at time t after burning, α is the absorption coefficient, L the sample length, T_{1e} and T_{1b} are the T_1 lifetimes of the excited and bottleneck states, respectively, and $B = (\beta/2)T_b/(T_b - T_e)$ identifies the branching ratio β . We find the time-dependent population difference to be characterized by a fast exponential decay with a lifetime of $T_{1e} = 82 \pm 2 \mu$ s, and a slower exponential decay from 3F_4 , characterized by $T_{1b} = 2.364 \pm 0.198$ ms. Both decay constants agree with previous measurements [69]. Furthermore, we find a branching ratio of 0.436 ± 0.017 .

We also performed hole burning studies under application of magnetic fields between 100 and 1250 Gauss, oriented parallel to the crystal C_3 -axis. For these measurements, we increased the burning time to 500 ms, and varied the waiting time between 100 ms and 6 s so that population in the 3H_4 and 3F_4 levels could be ignored. As depicted in Fig. 9, this allowed the observation of spectral holes persisting during waiting times of up to seconds, with the decay of the hole depth being again well described by the sum of two exponentials. Furthermore, the two decay times change with magnetic field, as depicted in Fig. 10. This indicates the appearance of two magnetic field dependent atomic levels with long lifetimes, and suggests maximum lifetimes at magnetic fields around 600 G.

While we have not been able to identify the levels involved in the long-term storage, e.g. through the observation of additional holes or anti-holes that indicate field-induced level splitting [70], we believe that 3H_6 nuclear hyperfine levels play a role. Note that

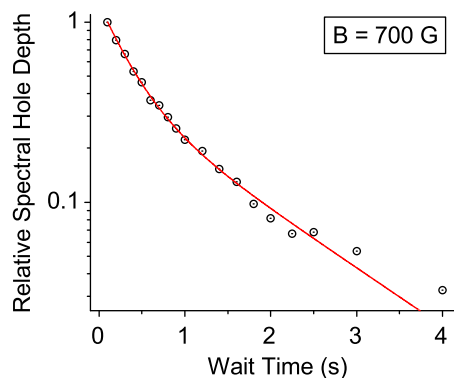


Fig. 9. Spectral hole depth as a function of the waiting time for a magnetic field of 700 G. The observation of two exponential decays indicates the existence of long-lived, ground state sub-levels.

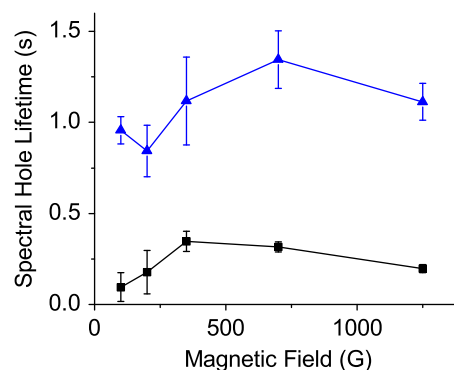


Fig. 10. Magnetic field dependence of the two decay times extracted from measurements of the spectral hole depth as a function of the waiting time. The case $B = 700$ G is shown in Fig. 9.

90 MHz splitting has been reported at 700 G [47]. We point out that the direct relaxation between different nuclear spin states in the excited and ground state multiplets is likely to be forbidden in the case where the magnetic field is parallel to the crystal C_3 -axis [39]. The observed long-lived storage thus probably involves a (spin mixing) relaxation pathway including the 3H_5 level. The role of superhyperfine interaction of thulium ions with neighboring lithium or niobium ions, leading to level splitting of ~ 1 MHz at 700 G [47], cannot be assessed from our measurements and requires more investigations.

Furthermore, relaxation between different ground states, which gives rise to the curves shown in Figs. 9 and 10, is likely to involve several contributions, including spin-lattice relaxation, spin-spin flip flops between neighboring Tm ions, or interactions of Tm ions with other magnetic impurities [71–76]. Further studies at different temperatures and with crystals with smaller Tm ion concentration are in progress.

To summarize this section, we have observed a short lifetime of the 3H_4 level compared to the 3F_4 , and the 3H_6 sub-levels. We have also identified a large branching ratio from 3H_4 to 3F_4 . These observations identify two potential approaches to spectral tailoring, either involving the bottleneck state (maybe taking advantage of stimulated emission [13,77]), or the magnetic field dependent ground states as an auxiliary state. In this context, the existence of the bottleneck state is of particular interest. Indeed, due to the large energy gap relative to the 3H_6 and 3H_4 electronic levels, population pumped into this state during spectral tailoring does not interact with light coupling the ground and excited states. This allows tailoring of the initial absorption line over a

spectral interval that is in principle only limited by the inhomogeneous broadening of the ${}^3\text{H}_6 \leftrightarrow {}^3\text{H}_4$ transition, and not by energy spacings in the ground or excited levels [11]. In other words, use of the bottleneck state for optical pumping could allow storage of short pulses of light with spectral widths exceeding GHz.

Furthermore, it may be possible to reversibly map optically excited coherence (on the ${}^3\text{H}_6 \leftrightarrow {}^3\text{H}_4$ transition) onto ${}^3\text{H}_6 \leftrightarrow {}^3\text{F}_4$ coherence, or long-lived ground state coherence. However, more investigations are required, for instance concerning the nature of the coupling between the ${}^3\text{H}_4$ and ${}^3\text{F}_4$ states, or the possibilities for a Raman transfer into ${}^3\text{H}_6$ ground states.

4.3. Optical coherence and spectral diffusion

For photon-echo quantum memories, the initial inhomogeneous absorption line must be tailored into one or more narrow lines using frequency-selective optical pumping. In the case of CRIB, the width of the resulting spectral feature determines the time quantum information can be stored in optical coherence [78]. For AFC, it determines the spacing of the teeth in the comb structure, which, in turn, sets the storage time in optical coherence [18]. Material dependent constraints to this time arise from the homogeneous line width Γ_{hom} , which is limited by the radiative lifetime: $\Gamma_{\text{hom}}^{\text{nat}} = 1/(2\pi T_{1e}) \approx 1.9$ kHz, phonon broadening [79], as well as long-term spectral diffusion [74,80,81].

To assess the short-term homogeneous line width, we employed two-pulse photon-echoes. Two 20 ns long pulses, with peak powers ~ 3 mW that maximized the observed echo, were sent into the thulium waveguide, and the relative delay was varied from 100 ns to 1.8 μs in steps of 25 ns. Fig. 11 depicts the resulting peak echo powers for the case of zero magnetic field. We fit the decay of the peak echo intensity I (which is proportional to power) with the Mims expression [82]:

$$I = I_0 \exp(-4t/T_2)^x \quad (2)$$

where I_0 denotes the maximum echo intensity, T_2 is the coherence time and x characterizes spectral diffusion. The fit revealed a coherence time of $1.580 \pm 0.008 \mu\text{s}$, equivalent to a homogeneous line width of ~ 200 kHz, and a spectral diffusion parameter x of 1.072 ± 0.009 . We obtained similar results for non-zero fields up to 250 Gauss. This indicates that the short-term homogeneous line width at 3 K is dominated by phonon scattering.

Beyond the short-term homogeneous line width, the narrowest spectral feature that can be generated through optical pumping is limited by spectral diffusion. Spectral diffusion is caused by fluctuations of each ion's transition frequency due to the dynamic nature of the ion's environment. This causes

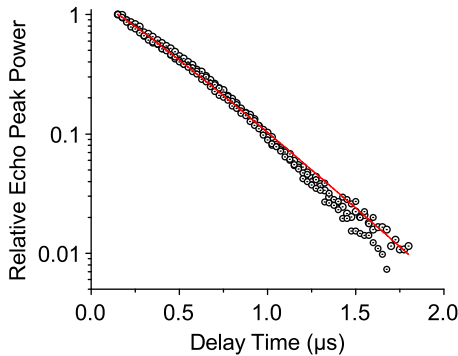


Fig. 11. Two pulse photon-echo peak powers measured under zero magnetic field. Plotted circles are normalized echo powers as a function of the delay time between the two pulses. Fitted is the Mims expression giving a coherence time of $1.6 \mu\text{s}$ with nearly absent spectral diffusion.

broadening of the homogeneous line width over time. The three pulse photon-echo (3PPE), or stimulated photon-echo, is a useful tool to investigate spectral diffusion [74].

We performed a series of 3PPE experiments to probe spectral diffusion in our sample. All experiments were carried out at zero magnetic field. In the measurements, for three different delay settings between the first two pulses, we varied the waiting time, i.e. the time between the second and the third pulse, from 1 to 400 μs with 5–10 μs increments. The echo peak power was measured for each delay and waiting time, and each set of measurements (i.e. measurements with a specific delay time) was normalized to the echo peak power at 1 μs waiting time. The results are illustrated in Fig. 12.

To interpret the data, we employed the spectral diffusion model discussed in Ref. [74]. In this model, the peak intensity I of the stimulated echo is determined by the relative dephasing during the delay time t_D , the decay of the excited level population during the waiting time t_W , and diffusion mechanisms which broaden the line into the time-dependent effective line width Γ_{eff} . In its general form, the 3PPE intensity can be written as

$$I(t_W, t_D) = I_0 F(t_W) \exp\{-4\pi t_D \Gamma_{\text{eff}}(t_D, t_W)\} \quad (3)$$

where I_0 denotes the maximum echo intensity, $F(t_W) = (1-B)\exp(-2t_W/T_{1e}) + B\exp(-2t_W/T_{1b})$ describes the population decay during t_W , and B is defined as in Eq. (1). The effective line width describes spectral diffusion during both the delay and waiting time, and is given by

$$\Gamma_{\text{eff}}(t_D, t_W) = \Gamma_0 + \frac{1}{2}\Gamma_{\text{SD}}[Rt_D + (1 - \exp(-Rt_W))] \quad (4)$$

where Γ_0 is the short-term line width in absence of spectral diffusion, and Γ_{SD} denotes the maximum additional line width due to spectral diffusion, which occurs at rate R .

To fit our data, we fixed the bottleneck level lifetime to 2.4 ms, obtained through the spectral hole burning measurements discussed above. This was required due to the echo intensity reaching the noise level after 200 μs , which is too short for the fit to generate a reliable lifetime. By setting $t_W = 0$, we extracted an intrinsic homogeneous line width of $\Gamma_0 = 152 \pm 2$ kHz via Eq. (3), in reasonable agreement with the result of ~ 200 kHz found via Eq. (2). Fitting all delay settings yielded an average excited level lifetime and branching ratio of $83 \pm 8 \mu\text{s}$ and 0.23 ± 0.03 , respectively, in reasonably good agreement with the more reliable values obtained from the spectral hole burning measurements.

Furthermore, the fit yielded $\Gamma_{\text{SD}} = 930 \pm 51$ kHz and a spectral diffusion rate of 227 ± 24 kHz, and the diffusion model thus predicts that the effective line width

$$\Gamma_{\text{eff}}(t_W) = \Gamma_0 + \frac{\Gamma_{\text{SD}}}{2}[1 - \exp\{-Rt_W\}] \quad (5)$$

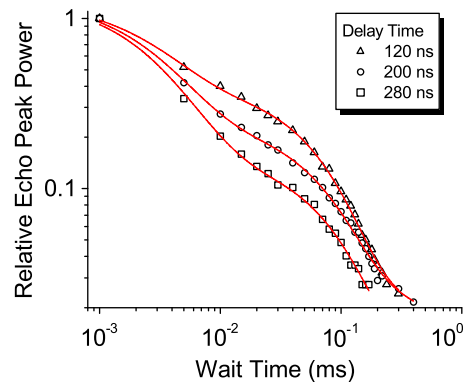


Fig. 12. Decay of stimulated echo with waiting time for delay times of 120 ns (triangle), 200 ns (circle) and 280 ns (square), respectively.

saturates at around 630 kHz after a waiting time of $\sim 50 \mu\text{s}$. When assessed through spectral hole burning, this leads to a homogeneous line width of $\Gamma_0 + \Gamma_{SD} = 1082 \text{ kHz}$ [83].

To verify this prediction, we performed another series of spectral hole burning measurements with burning and waiting times of 5 and $50 \mu\text{s}$, respectively. Varying the power of the burning pulse from 400 to $4 \mu\text{W}$, and extrapolating the hole width to zero burning power [84], we find a homogeneous line width of $1.5 \pm 0.1 \text{ MHz}$. Taking into account laser frequency jitter of $\sim 1 \text{ MHz}$, this is consistent with the prediction from the spectral diffusion model.

Summarizing these results, we have identified spectral diffusion as the limiting factor for storage of quantum information in optical coherence in Ti: Tm: LiNbO₃. For instance, assuming an AFC with 3 MHz teeth spacing, the storage time in optical coherence would be limited to $\sim 300 \text{ ns}$. We expect that the application of a magnetic field and the decrease of temperature will lead to an improvement of the short-term line-width along with a reduction of spectral diffusion, similar to what has been observed for Tm: LiNbO₃ bulk crystals [48].

4.4. Stark effect

Electric field control can constitute a key ingredient in photon-echo quantum memory and quantum information processing. It enables controlled manipulation of resonance frequencies of absorbers for storage and recall, e.g. for controlled reversible inhomogeneous broadening of narrow absorption lines in CRIB, and quantum state engineering such as pulse compression/decompression [85]. This control is governed by the interaction of applied external fields with permanent electric dipole moments. Provided the dipole moment is different for the ground and excited state, a shift in the resonance frequency $\Delta\omega$ occurs:

$$\Delta\omega = \frac{\chi}{\hbar} \Delta\vec{\mu}_e \cdot \vec{E} \quad (6)$$

where $\Delta\vec{\mu}_e$ denotes the difference in electric dipole moments for the states connected by the probe light, \vec{E} is the applied electric field, and χ is the Lorentz correction factor. This is also known as the DC Stark effect [51].

To observe the frequency shift for different electric fields, we first burned a spectral hole, then applied a variable voltage parallel to the crystal C₃-axis, and assessed the displacement of the hole using a weak, chirped, read pulse, as detailed in Ref. [52].

As shown in Figs. 13 and 14, we observe a linear frequency shift of $24.6 \pm 0.7 \text{ kHz cm/V}$. For example, an electric field of 100 V/mm leads to a displacement of the resonance frequency by 25 MHz. In the case of a Tm waveguide, where electrodes can be

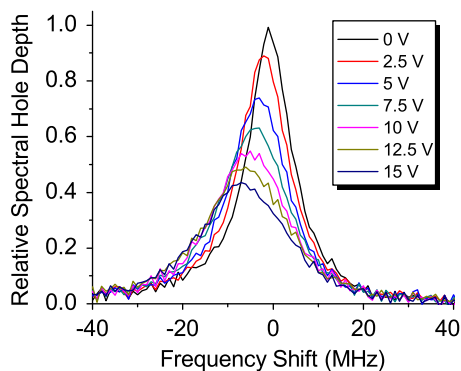


Fig. 13. Change of a spectral hole under application of different voltages. We attribute the broadening of the spectral hole with increased voltage to the large inhomogeneity of the electric field at the beginning and end of the LiNbO₃ waveguide.

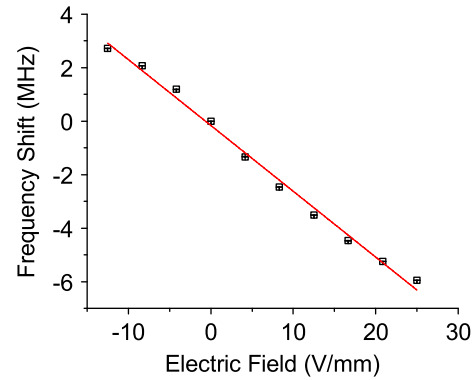


Fig. 14. Shift of transition frequency of the center of a spectral hole as a function of applied electric field, yielding a shift of $24.6 \pm 0.7 \text{ kHz cm/V}$.

spaced as closely as $10 \mu\text{m}$, this requires the application of 1 Volt. Since low voltages can be switched rapidly with ease, waveguides provide the ability to reversibly broaden and manipulate absorbers within hundreds of picoseconds.

5. Discussion and conclusion

To conclude, our findings demonstrate the suitability of Ti: Tm: LiNb₃ waveguides cooled to 3 K for implementations of photon-echo quantum memory protocols. Level structure, lifetimes, and branching ratios allow tailoring of the natural, inhomogeneously broadened absorption profile—either via optical pumping into the 3F_4 bottleneck state (then possibly allowing storage of nanosecond pulses), or into one of the long-lived ground states that appear under the application of magnetic fields. The minimum width of spectral holes of around one MHz, as determined by spectral diffusion, will limit storage of quantum information in optical coherence to roughly a hundred nanoseconds. While longer times may be achievable at lower temperature, this is still sufficient for mapping coherence onto long-lived ground state coherence, as Rabi frequencies exceeding hundred MHz can be obtained, due to the high power densities achievable inside waveguiding structures. We point out that ground state coherence of $300 \mu\text{s}$ has been reported for Tm:YAG [43], but investigations for Ti: Tm: LiNbO₃ remain to be done. Finally, the existence of a linear Stark shift, together with the possibility to space electrodes closely, allows shifting of resonance frequencies by more than 100 MHz within sub-nanosecond times, thus enabling novel phase control techniques.

Interestingly, the lifetimes and branching ratio found in our study differ from those reported for Tm: LiNbO₃ bulk crystals probed at 794.22 nm wavelength and 1.7 K [47,48]. The difference could be due to the addition of titanium to our sample, which may alter radiative or non-radiative decay channels [53], to wavelength-dependent spectroscopic properties as suggested in [48], or to concentration dependence [86].

Finally, we point out that RE doped waveguides, here Ti: Tm: LiNbO₃, are not only interesting for quantum state storage using a photon-echo approach, but also for other approaches, e.g. based on electromagnetically induced transparency and slow light [4].

Acknowledgments

WT gratefully remembers discussions with Drs. Olivier Guillot-Noël, Ivan Lorgère, and Thierry Chanelière starting with a visit in Paris in Spring 2007, which triggered the investigations

reported in this article. Furthermore, the authors thank Drs. Rufus Cone and Charles Thiel for enlightening discussions on properties of $Tm : LiNbO_3$, in particular for their groundbreaking work first reported at a workshop 2008 in Bozeman. We also thank Dr. Hubertus Suche for help regarding the waveguide characterization, and Vladimir Kiselyov for technical support. Financial support by NSERC, GDC, iCORE, AET and CFI is acknowledged.

References

- [1] N. Sangouard, et al., arXiv:0906.2699.
- [2] P. Kok, et al., *Rev. Mod. Phys.* 79 (2007) 135.
- [3] K. Hammerer, A.S. Sørensen, E.S. Polzik, arxiv:0807.3358, *Rev. Mod. Phys.*, accepted for publication.
- [4] A.I. Lvovsky, B.C. Sanders, W. Tittel, *Nat. Photon.* 3 (2009) 706.
- [5] W. Tittel, et al., *Laser & Phot. Rev.* DOI 10.1002/lpor.200810056.
- [6] W.H. Hesselink, D.A. Wiersma, *Phys. Rev. Lett.* 43 (1979) 1991.
- [7] T. Mossberg, *Opt. Lett.* 7 (1982) 77.
- [8] M. Mitsunaga, R. Yano, N. Uesugi, *Opt. Lett.* 16 (4) (1991) 264.
- [9] M. Mitsunaga, *Opt. Quant. Elect.* 24 (1992) 1137.
- [10] G.J. Pryde, M.J. Sellars, N.B. Manson, *Phys. Rev. Lett.* 84 (2000) 1152.
- [11] M. Nilsson, et al., *Phys. Rev. B* 70 (2004) 214116.
- [12] V. Crozatier, et al., *Opt. Comm.* 241 (2004) 203.
- [13] B. Lauritzen, et al., *Phys. Rev. A* 78 (2008) 043402.
- [14] S. A. Moiseev, S. Kröll, *Phys. Rev. Lett.* 87 (2001) 173601.
- [15] M. Nilsson, S. Kröll, *Opt. Comm.* 247 (2005) 292.
- [16] A.L. Alexander, et al., *Phys. Rev. Lett.* 96 (2006) 043602.
- [17] B. Kraus, et al., *Phys. Rev. A* 73 (2006) 020302(R).
- [18] M. Afzelius, et al., *Phys. Rev. A* 79 (2009) 052329.
- [19] H. de Riedmatten, et al., *Nature* 456 (2008) 773.
- [20] G. Hétet, et al., *Phys. Rev. Lett.* 100 (2008) 023601.
- [21] M. Afzelius, et al., arXiv:0908.2309.
- [22] G. Hétet, et al., *Opt. Lett.* 33 (2008) 2323.
- [23] S.A. Moiseev, W. Tittel, arXiv:0812.1730.
- [24] J.-L. Le Gouët, P.R. Berman, arXiv:0904.0667.
- [25] M. Hosseini, et al., *Nature* 461 (2009) 241.
- [26] T. Chanelière, et al., arXiv:0902.2048.
- [27] A. Amari, et al., arXiv:0911.2145.
- [28] M. Hedges, et al., Poster presentation at the International Conference on Hole Burning, Single Molecule, and Related Spectroscopies: Science Applications (HBSM 2009), Palm Cove, Australia, June 2009.
- [29] I. Usmani, et al., unpublished.
- [30] E. Fraval, M.J. Sellars, J.J. Longdell, *Phys. Rev. Lett.* 95 (2005) 030506.
- [31] P.J. Kwiat, et al., *Phys. Rev. Lett.* 75 (1995) 4337.
- [32] G. Ribordy, et al., *Phys. Rev. A* 63 (2001) 012309.
- [33] M. Halder, et al., *Opt. Express* 17 (2009) 4670.
- [34] J. Slater, et al., arXiv:0908.3516.
- [35] See PerkinElmer single photon counting modules <<http://optoelectronics.perkinelmer.com>>.
- [36] J. Gruber, et al., *Phys. Rev. B* 40 (1989) 9464.
- [37] M. Tian, et al., *J. Opt. Soc. Amer. B* 18 (2001) 673.
- [38] M. Ohlsson, et al., *Opt. Lett.* 28 (2003) 450.
- [39] O. Guillot-Noël, et al., *Phys. Rev. B* 71 (2005) 174409.
- [40] P. Goldner, et al., *Opt. Mater.* 28 (2006) 649.
- [41] F. de-Seze, et al., *Phys. Rev. B* 73 (2006) 85112.
- [42] A. Louchet, et al., *Phys. Rev. B* 75 (2007) 35131.
- [43] A. Louchet, et al., *Phys. Rev. B* 77 (2008) 195110.
- [44] R. Macfarlane, *Opt. Lett.* 18 (22) (1993) 1958.
- [45] L. Núñez, et al., *J. Lumin.* 55 (1993) 253.
- [46] R.K. Mohan, et al., *J. Lumin.* 127 (2007) 116.
- [47] C.W. Thiel, et al., Workshop on the Storage and Manipulation of Quantum Information in Optically-Addressed Solids, Bozeman, Montana, January 2008.
- [48] C.W. Thiel, et al., *J. Lumin.*, this issue.
- [49] T. Chanelière, et al., arXiv:0911.3328.
- [50] D.N. Nikogosyan, *Nonlinear Optical Crystals: A Complete Survey*, Springer, Berlin, 2005.
- [51] R. Macfarlane, *J. Lumin.* 125 (2007) 156.
- [52] S.R. Hastings-Simon, et al., *Opt. Comm.* 266 (2006) 716.
- [53] V. Dierolf, et al., *Appl. Phys. B* 72 (2001) 803.
- [54] Y. Sun, et al., *J. Lumin.* 98 (2002) 281.
- [55] M. Colice, F. Schlottau, K.H. Wagner, *Appl. Opt.* 45 (2006) 6393.
- [56] Y.N. Korkishko, et al., *Appl. Opt.* 35 (1996) 7056.
- [57] R.V. Schmidt, I.P. Kaminov, *Appl. Phys. Lett.* 25 (1974) 458.
- [58] E.L. Wooten, et al., *IEEE J. Sel. Top. Quant. Electron* 6 (2000) 1.
- [59] S. Tanzilli, et al., *Nature* 437 (2005) 116.
- [60] M. Staudt, et al., *Phys. Rev. Lett.* 98 (2007) 113601.
- [61] M. Staudt, et al., *Phys. Rev. Lett.* 99 (2007) 173602.
- [62] A. Delfan-Abazari, et al., arXiv:0910.2457.
- [63] H. Bubert, H. Jenett, *Surface and Thin Film Analysis*, Wiley-VCH, 2002 ISBN: 9783527304585.
- [64] M. Quintanilla, et al., *Opt. Mater.* 30 (2008) 1098–1102.
- [65] Baumann, et al., *Appl. Phys. A* 64 (1997) 33–44.
- [66] R. Regener, W. Sohler, *Appl. Phys. B* 36 (1985) 143–147.
- [67] E. Cantelar, et al., *J. Lumin.* 128 (2008) 988.
- [68] L.F. Johnston, A.A. Ballman, *J. Appl. Phys.* 40 (1969) 297.
- [69] E. Cantelar, et al., *Phys. Scripta T* 118 (2005) 69.
- [70] R.M. Macfarlane, R.M. Shelby, in: W.E. Moerner (Ed.), *Persistent Spectral Hole Burning: Science and Applications*, Springer, Berlin, 1988.
- [71] D.A. Davids, P.E. Wagner, *Phys. Rev. Lett.* 12 (1964) 141.
- [72] G.H. Larson, C.D. Jeffries, *Phys. Rev.* 141 (1966) 461.
- [73] I.N. Kurkin, K.P. Chernov, *Physica B & C* 233 (1980) 101.
- [74] T. Böttger, et al., *Phys. Rev. B* 73 (2006) 075101.
- [75] S.R. Hastings-Simon, et al., *Phys. Rev. B* 77 (2008) 125111.
- [76] S.R. Hastings-Simon, et al., *Phys. Rev. B* 78 (2008) 085410.
- [77] G. Gorju, et al., *J. Phys.: Condens. Matter* 19 (2007) 386226.
- [78] N. Sangouard, et al., *Phys. Rev. A* 75 (2007) 032327.
- [79] R.S. Meltzer, in: G. Liu, B. Jacquier (Eds.), *Spectroscopic Properties of Rare Earths Optical Materials*, Springer, Berlin, 2005.
- [80] W.B. Mims, K. Nassau, J.D. McGee, *Phys. Rev.* 123 (1961) 2059.
- [81] Y.S. Bai, M.D. Fayer, *Phys. Rev. B* 39 (1989) 11066.
- [82] W. Mims, *Phys. Rev.* 168 (1968) 370.
- [83] M. Staudt, et al., *Opt. Comm.* 266 (2006) 720.
- [84] E.S. Maniloff, et al., *Chem. Phys.* 193 (1995) 173.
- [85] S.A. Moiseev, W. Tittel, in preparation.
- [86] M. Quintanilla, et al., *J. Lumin.* 128 (2008) 927.